JOURNAL OF MATERIALS SCIENCE 32 (1997) 2191–2206

Microstructural stability and mechanisms of fatigue and creep crack growth in Ti–24Al–11Nb

P. B. ASWATH, R. D. GOOLSBY AND L. W. GRAHAM
Department of Mechanical and Aerospace Engineering and Materials Science and Engineering Program, University of Texas at Arlington, Arlington, Texas 76019 USA

Titanium intermetallics are being developed for long term applications at elevated temperatures, particularly those alloys based on the alloys Ti_3Al and TiAl. Typical approaches include the design of appropriate microstructures for room and elevated temperature fatigue and creep resistance. However, a little explored area is the stability of these microstructures at elevated temperature and its effect on fatigue crack growth. The present investigation documented the microstructural stability, fatigue crack behaviour, and stress rupture of Ti–24Al–11Nb, a Nb modified Ti_3Al alloy. A coarse two phase $\alpha_2+\beta$ Widmanstätten microstructure was found to exhibit the best resistance to fatigue crack growth. Microstructural stability and elemental segregation were studied as a function of exposure time for up to 500 h at 800°C using transmission electron microscopy (TEM). Results indicate that the Widmanstätten microstructure is metastable and the β phase breaks up into particles. The absence of a continuous β phase surrounding the α_2 phase reduces the resistance of the microstructure to fatigue crack growth at room temperature. At elevated temperature the microstructure stability does not play a role in determining the fatigue resistance. A fine Widmanstätten microstructure has the best resistance to creep deformation. Stress rupture tests were conducted in vacuum and air at 649°C and 760°C. Two types of failure mechanisms were seen in stress rupture; these include transgranular and intergranular failure within prior β grains. When tested in air at 760°C a combination of transgranular and intergranular failure occurred. Specimens that exhibited a higher proportion of transgranular failure had longer lives. When tested in vacuum at 760°C the predominant failure mode was intergranular. At 760 °C extensive microstructural changes like breakup and spherodization of the β phase occurred under stress while the rate of coarsening without any stress was much slower. At 649°C the specimens tested in vacuum consistently exhibited longer lives. The creep crack growth when tested in air at 649 °C was always a brittle transgranular mode while the specimens tested in vacuum always failed by an intergranular mode.

1. Introduction

With the ongoing search for better materials with good high temperature properties and acceptable room temperature strength and toughness, titanium aluminide intermetallics have shown attractive promise [1–10]. Binary alloys based on the composition Ti_3Al and TiAl have been extensively studied. A major drawback of these systems is their poor ductility at room temperature, a consequence of their strong interatomic bonding and ordered structure.

Below 700 °C Ti_3Al exhibits predominantly planar slip, with slip vectors restricted to $\frac{a}{3}\langle 1120\rangle$ on basal and prism planes. The addition of Nb to the Ti_3Al alloy stabilizes the high temperature β phase which is more ductile than the brittle, low temperature α_2 phase. Most of the mechanical properties, except creep, appear to improve with the addition of Nb. Recent work [11, 12] has indicated that microstructure plays an important role in fatigue crack growth characteristics. In particular they noted that a coarse Widmanstätten structure yielded the best resistance to crack growth at room temperature. The presence of a continuous layer of the more ductile β phase around the α_2 appears to improve the resistance to crack growth. They also noted that at elevated temperatures the microstructure played a small role in influencing fatigue crack growth characteristics and other variables like oxidation and oxygen and hydrogen embrittlement play a significant role.

Most studies done so far in titanium aluminides have involved developing a certain microstructure and evaluating its properties under a variety of mechanical and thermomechanical conditions [12, 13]. The titanium intermetallics being developed typically find applications at temperatures of the order of 600–800 °C. Typical applications can be as long as 500 h at temperature. The metastable nature of the microstructures in titanium intermetallics can potentially lead to

0022–2461

significant changes in the microstructures at operational temperatures when diffusion aided processes are dominant. Therefore, results obtained from studies of the mechanical response of the alloys at room temperature or at select high temperatures alone may not reflect the true mechanical characteristics of the alloy in service.

The objective of this study was to evaluate the microstructural stability of a Ti–Al–Nb alloy subjected to prolonged exposure to elevated temperature and to assess the effects of such exposures on subsequent room and elevated temperature fatigue behaviour and stress rupture response. For this purpose, the coarse Widmanstätten microstructure of the Ti–24Al–11Nb (at %) alloy, which proved to have the best resistance to subcritical fatigue crack growth in an earlier study [11, 12], was chosen. Its stability on prolonged exposure at 800 °C for 0, 96, 250 and 500 h was examined using analytical electron microscopy. The exposed specimens were tested under fatigue loading conditions at room and elevated temperature. In addition a fine Widmanstätten structure was designed for the stress rupture and companion tensile tests. Tests were conducted in both air and vaccum at 649 °C and 760 °C. The results of this investigation are presented in this paper which is organized in the following manner. Section 2 provides details of the materials and test methods. Section 3 discusses the microstructural stability of the Widmanstätten microstructure after sucessively longer exposures at 800 °C. Section 4 concerns the room and elevated temperature fatigue crack growth behaviour. Section 5 details the results of the tensile and stress rupture tests. Key conclusions are listed in section 6.

2. Experimental procedures

2.1. Materials

The intermetallic alloy used in this investigation had a composition of 66.4 wt% Ti, 13.8 wt% Al, 19.7 wt% Nb, 0.057 wt% 0, 0.05 wt% Fe, 0.01 wt% N, and 0.02 wt% C (nominal Ti–24.2 at% Al–10.1 at% Nb). The alloy was produced at Alcoa Technical Laboratory, PA, by casting and drop forging into the shape of a pancake, approximately 260 mm in diameter and 11–12 mm in thickness.

2.2. Microstructural characterizations

Optical metallography was performed on all the microstructures to examine the stability. Three mm discs were punched out and dimpled and electropolished at 15V and 200 mA in 23% nitric acid in methanol at − 30 °C. Analytical electron microscopy was conducted on a Philips EM420, operating at 120 kV. Energy dispersive analysis was conducted on the different regions to study the segregation of elements.

2.3. Fatigue crack growth tests

The geometry of the fatigue crack growth specimens were *C–L* (circumferential–longitudinal) orientation, with the plane of the notch parallel to the forging direction of the pancake structure and the circular cross-section being normal to the plane of the notch. Fig. 1 is a schematic representation of the specimen orientation. The overall dimensions of the specimens were: length = 50 mm, width = 9.9 mm, and thickness between 5.0 and 6.35 mm. The ratio of the notch length to specimen width was 0.4. The base material specimens were given a 0.5 h heat treatment at 1093 °C followed by a fan air cool, which yields a coarse Widmanstätten microstructure. In addition to the baseline condition, additional specimens were subsequently subjected to four exposure times (96, 100, 250 and 500 h) at 800 °C in an air environment. These various heat treatment conditions are identified as A, B, B1, B2 and B3, as detailed in Table I (along with heat treatments prescribed for stress rupture tests). Care was taken to remove the oxygen affected zone before matching the samples. Through-thickness, mode I fatigue precracks were introduced by applying uniaxial cyclic compression loads at a constant cyclic frequency of 20 Hz in the laboratory environment in the edge notch configuration, following the procedure detailed in refs [8, 14]. The saturation length of the compression fatigue prepacks can be controlled between 0.2 mm and 1.4 mm by judicious selection of far-field cyclic compression loads.

Fatigue crack growth experiments at room temperature were conducted on four point bend specimens

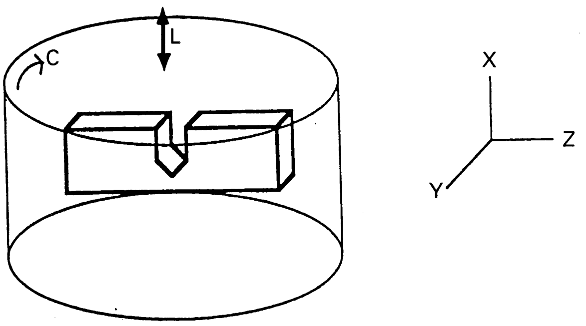

Figure 1 Geometry of the forging and fatigue crack growth specimen orientation.

TABLE I Details of the heat treatments used to condition specimens for fatigue crack growth and stress rupture tests

Test type	Name	Heat treatment
	A	1093 °C 1/2 h fan air cool
Fatigue	B	1093 °C 1/2 h fan air cool + 100 h at 800 °C, air cool
Crack	B1	1093 °C 1/2 h fan air cool + 96 h at 800 °C, water quench
Growth	B2	1093 °C 1/2 h fan air cool + 250 h at 800 °C, water quench
	B3	1093 °C 1/2 h fan air cool + 500 h at 800 °C, water quench
Stress	C	1148 °C 1/2 h fan air cool + 5 h. at 649 °C air cool
Rupture	D	1148 °C 1/2 h fan air cool + 5 h at 649 °C air cool + 5 h at 760 °C in 2×10^{-6} vacuum with furnace cool

which were heat treated to A, B1, B2 and B3 conditions. These four point bend specimens were the same edge notch specimens precracked in compression. Following precracking in cyclic compression, cyclic tensile loads were applied to the specimen for fatigue crack growth characterization using an Instron servohydraulic machine. Fig. 2 details the testing procedure. All fatigue tests were conducted at a load ratio ($P_{\mathrm{min}}/P_{\mathrm{max}} = R$) of 0.1 and a frequency of 20 Hz with a sinusoidal were form. In all the room temperature fatigue crack growth tests an initial stress intensity factor range ΔK of 1 MPa m$^{1/2}$ was applied to the specimen. The crack length was monitored with the aid of a travelling microscope (magnification of 400X) connected with a television camera and a video casette recorder. If no crack growth was observed after 200 000 cycles, the far-field ΔK was increased by 0.25 MPa m$^{1/2}$. This procedure was repeated until the fatigue threshold stress intensity factor range ΔK_{th} at which initiation of crack growth was detected. Beyond this threshold, the fatigue tests were conducted at a constant value of far-field cyclic loads, i.e. increasing ΔK. Plots of $\mathrm{d}a/\mathrm{d}N$ versus ΔK for the four heat treatments were made, where $\mathrm{d}a/\mathrm{d}N$ = crack growth rate per cycle in mm cycle^{-1} and $\Delta K = K_{\mathrm{max}} - K_{\mathrm{min}}$, with K = linear elastic stress intensity factor in units of MPa m$^{1/2}$ and K_{max} is the stress intensity factor at the maximum load and K_{min} is the stress intensity factor at the minimum load. Crack closure was monitored in two ways, the first technique involved using strain gauges on the specimen surface, above and below the crack plane, and monitoring the change in slope of the load versus strain plot to determine closure. This technique can only be used at room temperature. The second technique involved the use of a high powered microscope (400X) to monitor the crack faces and determine the load at which the crack faces meet. Closure was measured as $\Delta K_{\mathrm{cl}} = K_{\mathrm{max}} - K_{\mathrm{cl}}$, where K_{cl} is the stress intensity factor at the load when the crack faces meet.

Fatigue tests at 700 °C were also conducted for microstructures A and B in four point bend at a R-ratio of 0.1 at 20 Hz using an ATS air furnace with temperature tolerance of ± 2 °C. The crack length was monitored through the view port in the furnace using a Questar QM-1 telescope with a magnification of 200X. Due to the deleterious effect of temperature and environment, an initial stress intensity factor range ΔK of 6 MPa m$^{1/2}$ was applied. If no crack growth was seen after 100 000 cycles, the ΔK was increased by 10% and the test was continued till crack growth was seen, after which the far field load was kept constant, i.e. increasing ΔK.

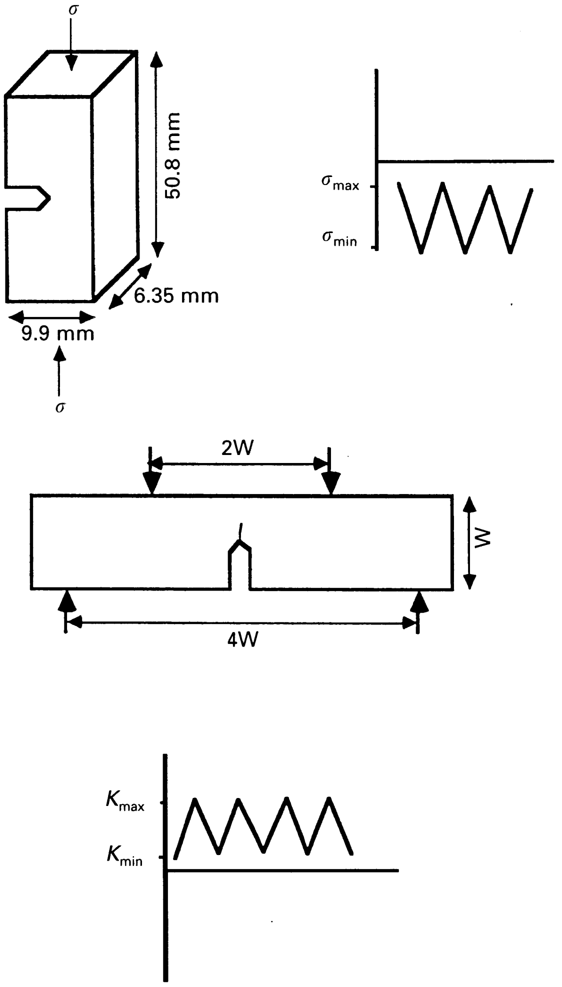

Figure 2 Fatigue crack growth specimen geometry, with precracking in cyclic compression and tensile fatigue testing in four point bending.

2.4. Stress rupture tests

Stress rupture tests and companion tensile tests were conducted at 649 °C and 760 °C using the specimen geometry detailed in Fig. 3. Specimens tested at 649 °C were subjected to heat treatment C prior to testing, while those tested at 760 °C were processed to heat treatment D prior to testing.

Vacuum stress rupture tests were conducted in a vacuum of 1×10^{-6} Torr. Heating was accomplished by a tungsten radiation heater and the temperature was controlled using a chromel-alumel thermocouple attached to the gauge section of the specimen. The specimen was heated at a rate of 17 °C per min to a temperature 55 °C below the desired test temperature, soaked 3–5 min and heated to the desired temperature at 17 °C per min. The specimen was soaked for 30 min at the desired temperature before the testing began. The temperature tolerance held by the controller was ± 2 °C. Loading was applied using a MTS servohydraulic test system in load control

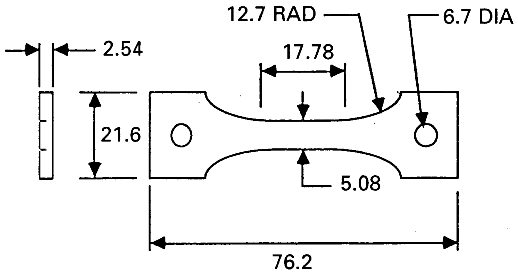

Figure 3 Specimen geometry for stress rupture tests and elevated temperature tensile tests.

mode. Before heating and during heating, a 3.5 MPa preload was applied and maintained to eliminate the possibility of any thermal expansion compressive loads. After heat up and temperature soak, the full load was gradually applied. Slight load fluctuations during the duration of the test resulted in stress variations of ± 2 MPa. Duplicate tests were conducted at each stress level.

Stress rupture tests in air were conducted in a Reihle creep test machine. The temperature was achieved using a Marshall tubular furnace with a heating rate of approximately 20 °C min^{-1}. A 45–60 min soak time was given at temperature before the loads were applied using dead weights. Tolerances of temperature were ± 4 °C. A minimum of two tests were performed at each stress level. The applied stress levels for all stress rupture tests (both air and vacuum) at 760 °C were nominally 137, 172, and 241 MPa. At the 649 °C test temperature the nominal applied stresses were 241, 310, 378, and 455 MPa.

The companion tensile tests used for correlation to the stress rupture tests were all conducted in vacuum using the same experimental setup described above. Duplicate tensile tests were conducted at 649 and 760 °C at a displacement rate of 0.43 mm min^{-1}.

3. Effects of elevated temperature exposure on microstructural stability

The as-received alloy had a heat treatment history of 30 min at 1093 °C followed by a fan air cool. A pseudo-binary phase diagram of the Ti_3Al–Nb system [15] is shown in Fig. 4. It has been suggested [6, 13] that a B2 phase with a CsCl structure and a stoichiometry of Ti_2AlNb exists in equilibrium with the α_2 phase between the β transus and 850 °C. Fan air cooling from this temperature range allows time for the B2 to $\alpha_2 + \beta$ transformation to occur. The heat treatment results in a coarse Widmanstätten microstructure with transformed β surrounding the α_2 phase continuously. In the present study the as-received alloy was subjected to a heat treatment of 30 min at 1093 °C followed by a fan air cool (identified in Table I as heat treatment A). Thus, a coarse Widmansätten microstructure was obtained via this heat treatment as shown in the Fig. 5(a), (b) which show optical and transmission electron micrographs.

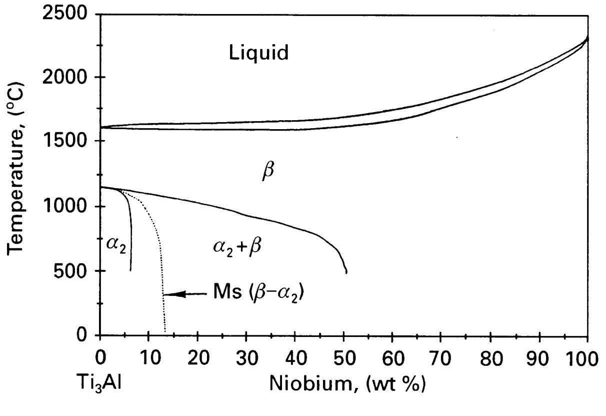

Figure 4 Pseudo-binary Ti_3Al–Nb phase diagram [15].

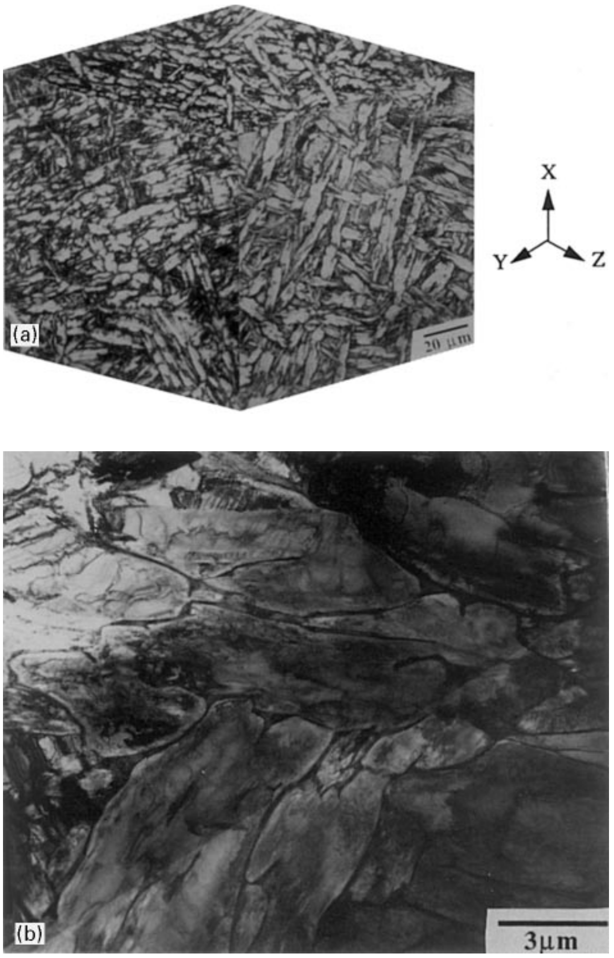

Figure 5 (a) Optical micrograph of the baseline heat treatment (A) with a coarse Widmanstätten microstructure (b) Bright field transmission electron micrograph showing the α_2 phase surrounded by a continuous β phase.

Earlier work by Aswath and Suresh [12] has indicated that this microstructure offers the best combination of room and elevated temperature fatigue crack growth resistance and thus this was chosen as the base microstructure for this investigation. In order to study the stability of the microstructure to long term exposure, specimens were then subsequently exposed for 96, 100, 250 and 500 h at 800 °C. The 96, 250 and 500 h exposure correspond to conditions B1, B2 and B3 in Table I for fatigue crack growth tests.

A 100 h exposure at 800 °C followed by an air cool (heat treatment B) leads to the break up of the continuous β phase surrounding the α_2. Fig. 6(a), (b) are optical and transmission electron micrographs of the microstructure. The laths of the α_2 no longer have sharp interfaces. Fig. 6c shows the presence of interfacial dislocations between the α_2 and β phases. These dislocations were not present in the base alloy corresponding to heat treatment A. Fig. 6d shows a low angle grain boundary between two α_2 laths. These dislocations take the place of the β phase which has dissolved due to the 100 h exposure at 800 °C. An energy dispersive analysis using X-rays of the α_2 and β phase in heat treatments A and B indicates that there is a large increase in the Nb content in the β phase in the heat treatment B sample as compared to the heat treatment A sample. (The energy dispersive

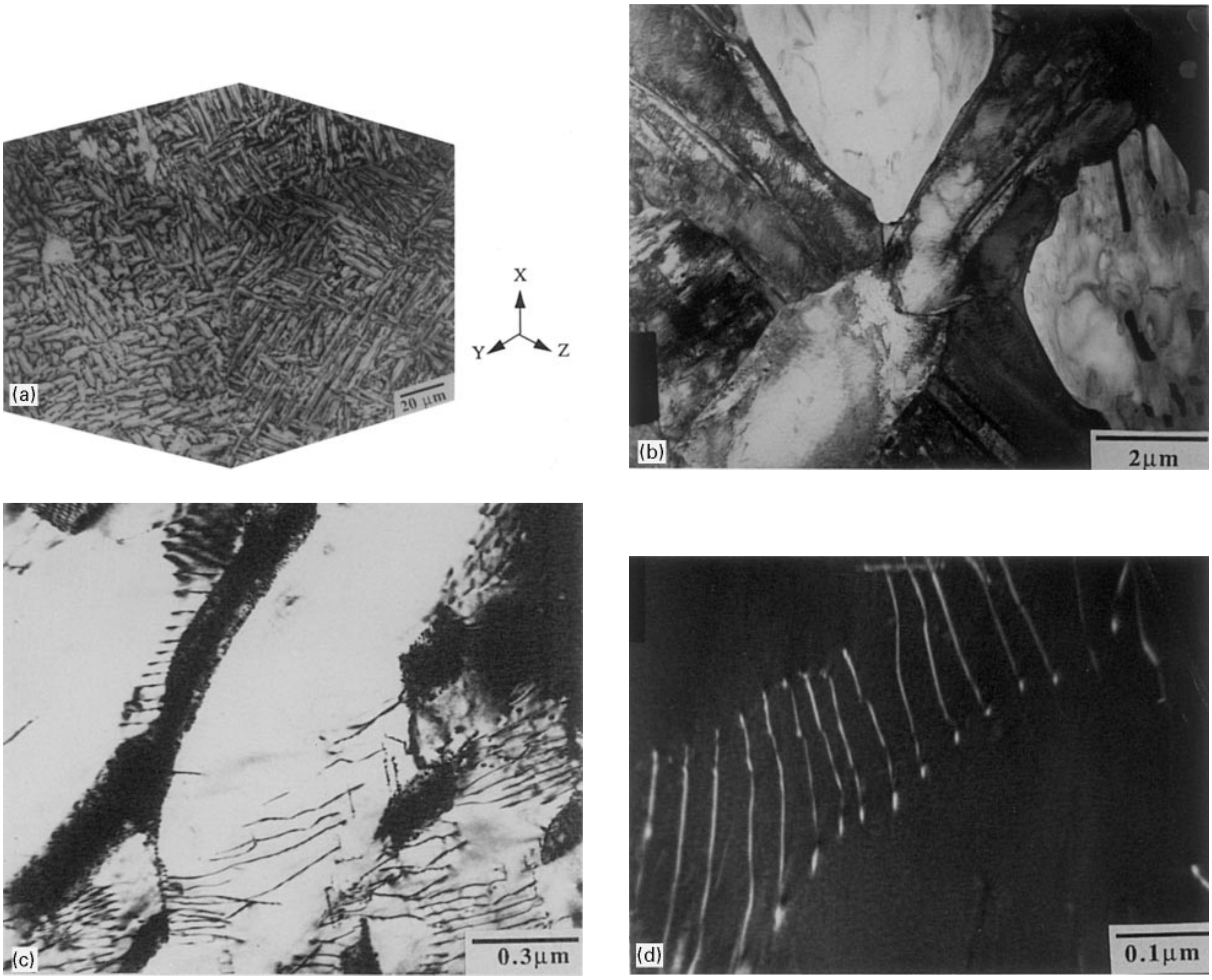

Figure 6 (a) Optical micrograph of the baseline alloy heat treated for 96 h at 800 °C followed by an air cool (B). The microstructure indicates that there is a breakup of the Widmanstätten microstructure (b) Bright field transmission electron micrograph showing the β phase break up. (c) High magnification bright field image showing the development of interfacial dislocations at the α_2/β interface. (d) High magnification dark field image showing parallel super dislocations within the α_2 indicating a low angle grain boundary separating neighbouring α_2 laths.

analysis was conducted using the spot mode in the transmission electron microscope and care was taken to ensure that there was no overlap of the α_2 and β phases.) Earlier works have indicated that the composition of the β phase is based on the intermetallic Ti_2AlNb [16]; however, our results indicate that the Nb content exceeds the Al content. It is postulated that the larger difference in lattice parameters between the α_2 and β phases in sample B leads to a semicoherent interface and hence the presence of a large number of interfacial dislocations. In regions where the β phase has dissolved, adjacent α_2 laths are now separated by an array of low angle grain boundary dislocations.

In order to preserve the microstructure developed due to exposure at elevated temperature all subsequent specimens were quenched after the high temperature exposure. A 96 h exposure at 800 °C followed by a cold water quench (heat treatment B1) yields a microstructure where there is a breakup of the Widmanstätten microstructure. The β phase is no longer continuous and exists as discrete particles. Fig. 7(a), (b) are the optical and transmission electron micrographs of heat treatment B1, respectively.

Heat treatments for 250 and 500 h at 800 °C followed by a cold water quench (heat treatments B2 and B3, respectively) lead to a further breakup of the β phase. Fig. 8a and Fig. 9a are optical micrographs and Fig. 8b, and Fig. 9b are bright field transmission electron micrographs of heat treatments B2 and B3, respectively. These micrographs indicate that the β phase is no longer a continuous phase surrounding the α_2 but is more like a ductile phase scattered in the α_2 matrix. The β phase is scattered along prior α_2/β boundaries and linked together with superlattice dislocations. These superlattice dislocations are in effect low angle grain boundaries separating neighbouring α_2 regions. It is important to note that even after 500 h at 800 °C the intermetallic has not developed a stable microstructure.

Heat treatment C (0.5 h at 1148 °C followed by a fan air cool + 5 h at 649 °C followed by an air cool) was chosen for the stress rupture experiments at 649 °C. Fig. 10 is an optical micrograph of the microstructure produced by this heat treatment. Key observations from this micrograph include: (i) region A is a complete prior β grain which is completely transformed to a fine basket weave Widmanstätten microstructure.

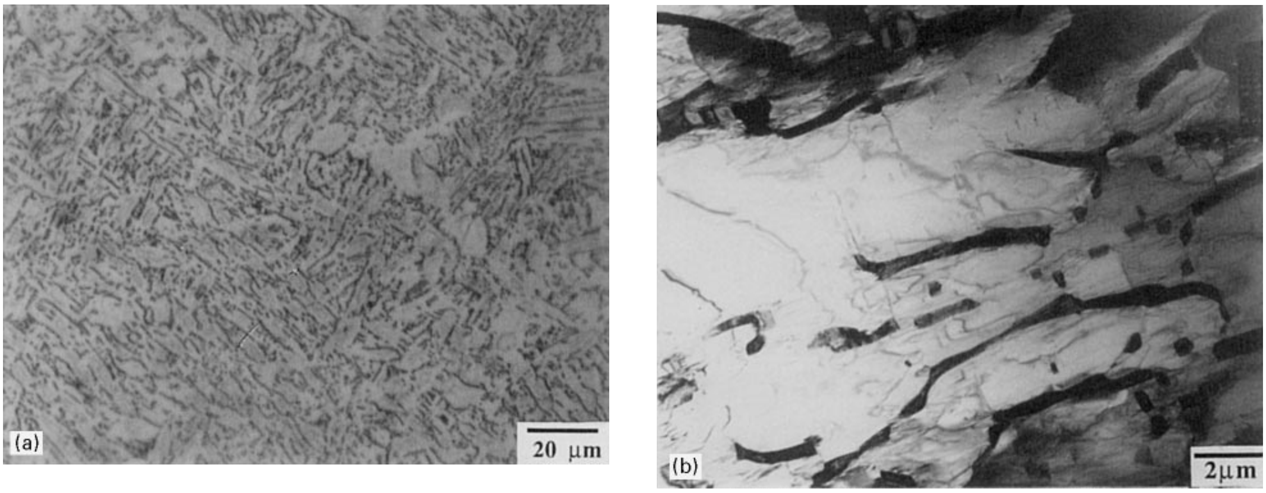

Figure 7 (a) Optical micrograph of the baseline alloy heat treated for 100 h at 800 °C followed by a water quench (B1). The microstructure indicates that there is a breakup of the Widmanstätten microstructure (b) Bright field transmission electron micrograph showing the breakup of the β phase.

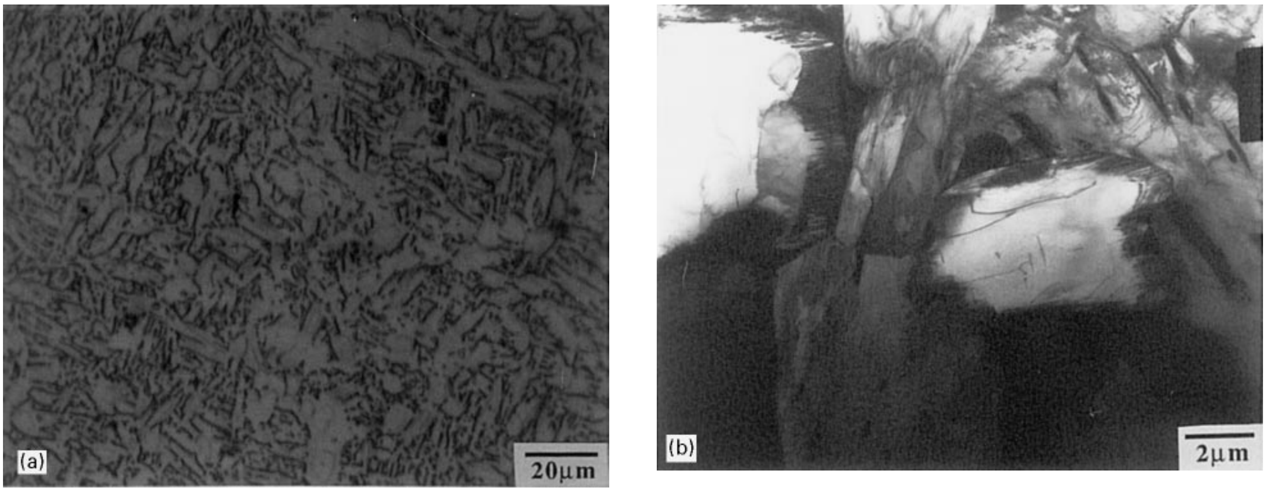

Figure 8 (a) Optical micrograph of the baseline alloy heat treated for 250 h at 800 °C followed by a water quench (B2). The microstructure indicates that there is a full breakup of the Widmanstätten microstructure (b) Bright field transmission electron micrograph showing the breakup of the β phase.

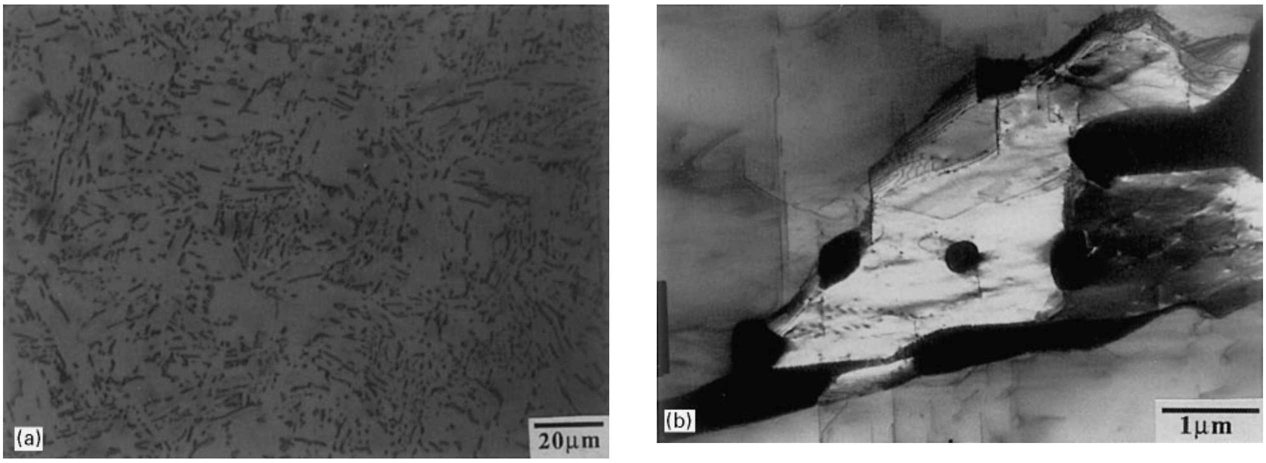

Figure 9 (a) Optical micrograph of the baseline alloy heat treated for 500 h at 800 °C followed by a water quench (B3). The microstructure indicates that there is a breakup of the Widmanstätten microstructure (b) Bright field transmission electron micrograph showing the spherodization of the β phase.

(ii) In grains labelled as B the microstructure is fine Widmanstätten structure with globular α_2. (iii) From region C it is clear that the Widmanstätten α_2 platelets have a preferred orientation relative to the prior β grain boundary. (iv) Region D indicates that globular α_2 exists at a prior β grain boundary. This microstructure is classified as Widmanstätten + grain boundary α_2. No preferred orientation was seen with

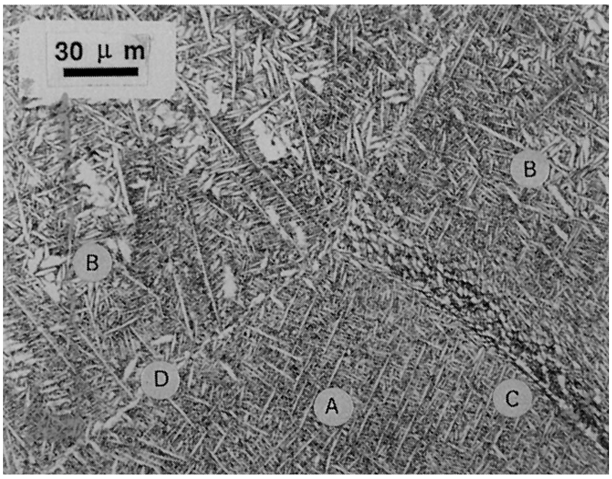

Figure 10 Optical micrograph of heat treatment C. See Table 1 for details of heat treatment. See text for descriptions of areas A through D.

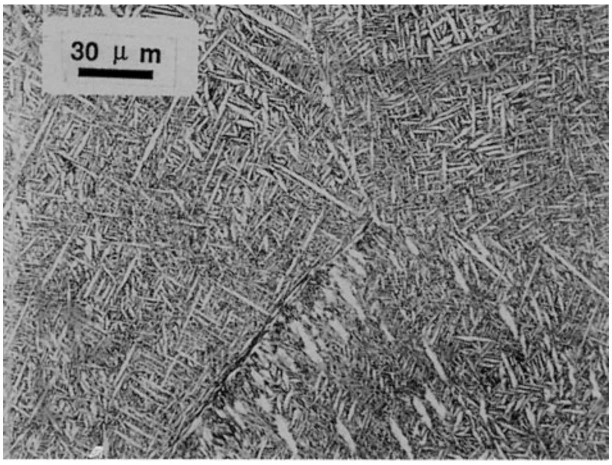

Figure 11 Optical micrograph of heat treatment D. See Table I for details of heat treatment.

respect to the forging operation. Microstructure D (1148 °C 0.5 h, fan air cool + 5 h at 649 °C air cool + 5 h at 760 °C in a vacuum of 3 x 10^{-6} followed by a furnace cool) is shown in Fig. 11. This microstructure is essentially the same as microstructure C. This heat treatment condition was selected for use in the 760 °C stress rupture evaluations.

4. Fatigue crack growth

4.1. Room temperature crack growth

Prolonged exposure at 800 °C results in a drastic decrease in the room temperature resistance to fatigue crack growth in the Paris regime. Fig. 12, is a plot of da/dN versus ΔK for the four heat treatments conditions detailed in Table 1 for increasing exposure time at 800 °C. The threshold for crack growth is only marginally decreased from 6 MPa m$^{1/2}$ for heat treatment A (0 h exposure) to 5.5 MPa m$^{1/2}$ for heat treatments B1 (96 h), B2 (250 h) and B3 (500 h). The level of closure is about the same for all the microstructures. Measurement of closure indicated that $\Delta K_{\mathrm{cl}} \approx 0.85\,\Delta K$. Hence d$a$/d$N$ versus ΔK provides a direct estimate of the intrinsic resistance of the microstructures to fatigue crack growth.

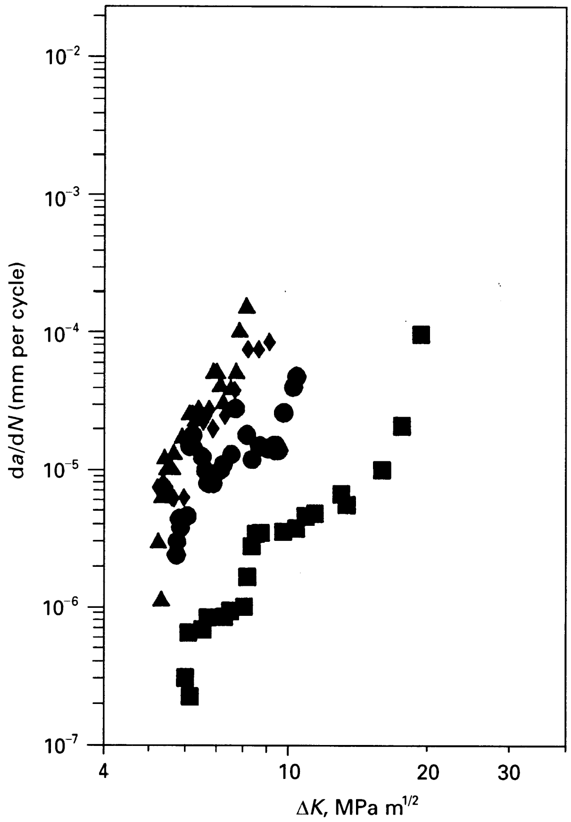

Figure 12 Fatigue crack growth rate da/dN as a function of stress intensity factor range ΔK at room temperature for Ti–24Al–11Nb alloy subjected to prior exposure at 800 °C for 0, 96, 250 and 500 h. All tests conducted at a frequency of 20 Hz and R = 0.1. with the (■) Heat treatments represented by; (■) A, (▲) B, (●) C and (◆) D, respectively.

It is clear that the rate of crack growth in the Paris regime is one to two orders of magnitude faster in the specimens that were exposed at 800 °C for long periods of time compared to specimens receiving no exposure at 800 °C (heat treatment A). Fig. 13(a, b) are the fatigue crack profiles of heat treatments A and B3 microstructures respectively, tested at room temperature. The crack profile in heat treatment A indicates that there is a periodic deflection of the crack. The crack encounters a deflection every time it encounters the β phase. In addition the more ductile β phase blunts the crack tip and improves resistance to crack growth. In heat treatment A the fracture morphology is primarily cleavage in the α_2 region and the cleavage facet size is dictated by the α_2 lath size, as revealed by scanning electron fractography. The β phase exhibits a quasi-cleavage appearance with a larger amount of plastic deformation. In the other three microstructures which resulted from 800 °C exposure prior to testing, the fatigue crack does not encounter as much resistance as it moves from one α_2 lath to the next, since the ductile β phase has dissolved from the boundary regions. The α_2 laths are still separated by low angle boundaries and hence there is a change in crack path as it passes from one α_2 lath to the next. This is the reason why the cleavage facet sizes in the fatigue fracture surface of specimens B1, B2 and B3 are not significantly different when compared to heat treatment A.

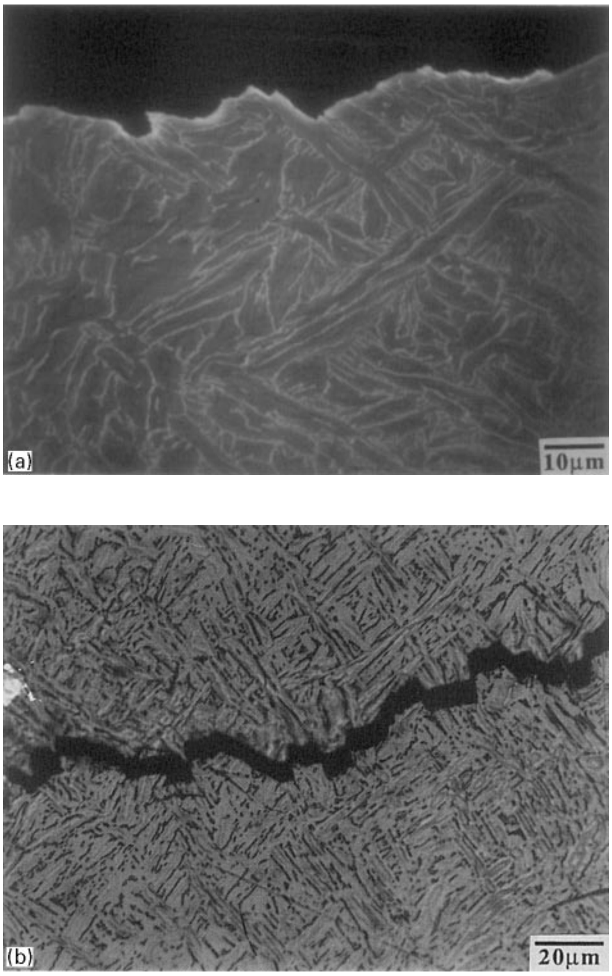

Figure 13 Optical micrograph of the fatigue crack profile for (a) Baseline microstructure (A) (b) Heat treatment B3 (exposed at 800 °C for 500 h prior to test). Both were tested at room temperature at a frequency of 20 Hz and $R = 0.1$.

4.1.1. Toughening by crack deflection

Estimation of the effects of crack deflection on the crack growth behaviour can be developed based on geometrical models discussed in detail in references [17, 18]. These models account for two effects which influence crack propagation rates of a periodically deflected crack. (i) The propagation of a fatigue crack with periodic changes in its path at the same rate as the corresponding straight crack of the same projected length requires an apparently larger driving force. (ii) A periodically deflected crack propagates at an apparently slower rate than a straight crack subjected to the same effective driving force.

In addition to the above mentioned effects an additional factor that affects fatigue crack growth characteristics arises from the mismatch between the mating fracture surface asperities. Measurements of closure using strain gauges do not truly represent the fatigue crack closure in the vicinity of the crack tip. Measurements made with a video camera and recorder provide better insights on the closure loads. (Both methods were employed in this study.) Analytical calculations based on simple geometrical models shown in Fig. 14, provide estimates of crack deflection and closure on the effective driving force of a periodically deflected crack [17, 18]. These are given by:

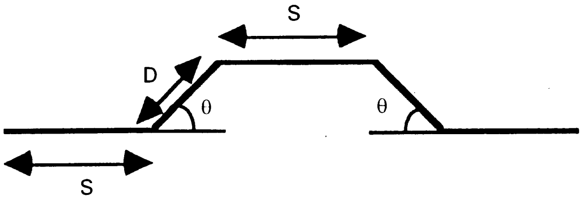

Figure 14 Fatigue crack deflection model [17, 18].

$$\Delta K_{\text{eff}} = \left(\frac{D\,\text{Cos}^2(\theta/2) + S}{D + S}\right) \times \left(1 - \left[\frac{X\tan\theta}{1 + X\tan\theta}\right]^{1/2}\right)\Delta K_{\text{app}}$$

where ΔK_{app} = applied stress intensity factor range, ΔK_{app} = effective stress intensity factor range after accounting for crack deflection and closure, θ is the (fixed) angle of periodic deflection away from the mode I growth plane, D is the distance over which the deflected crack advances along the branch or tilt in each segment, S is the distance over which a purely mode I fracture occurs in each segment, X is mismatch ratio, $X = u_{\text{II}}/u_{\text{I}}$, where u_{I} and u_{II} are mode I and II displacements along the crack faces, respectively. Furthermore, if the length of the deflected fatigue crack is measured along the mode I plane, the apparent crack growth rate, $(\text{d}a/\text{d}N)_{\text{app}}$ is related to the effective crack growth rate, $(\text{d}a/\text{d}N)_{\text{eff}}$, by the relationship:

$$\left(\frac{\text{d}a}{\text{d}N}\right)_{\text{eff}} = \left(\frac{\text{d}a}{\text{d}N}\right)_{\text{app}}\left(\frac{S + D\cos\theta}{D + S}\right)$$

In heat treatment A, crack deflection occurs via two means: (i) crack deflection at the α_2/β interface due to crack growth along the interface and (ii) crack deflection at the α_2/β interface as the crack passes from the α_2 to the β phase. The extent of crack deflection in both the above cases is dependent on the volume fractions of the α_2 and β phases and the presence of boundaries separating the α_2 laths. Based on a number of microscopic observations of crack profiles in the optical and scanning electron microscope, characteristic microscopic dimensions were chosen. In microstructure A, $\frac{D}{D+S} \cong 0.5$, and $\theta \approx 45^\circ$ yielding $\Delta K_{\text{eff}} = 0.93\ \Delta K_{\text{app}}$ when no closure is present and $\Delta K_{\text{eff}} = 0.65\ \Delta K_{\text{app}}$ when $X = 0.1$. Microstructures B1, B2 and B3 also exhibit similar levels of crack deflection as shown by the optical micrographs in Fig. 13, so similar estimates of $\frac{D}{D+S} \cong 0.5$, and $\theta \simeq 45^\circ$ can be used. Hence, the $\text{d}a/\text{d}N$ versus ΔK plot in Fig. 12 yields a good comparison of the intrinsic resistance of each of the microstructures to crack growth. It is apparent from Fig. 8 that on long term exposure to elevated temperature there is a significant reduction in the intrinsic resistance of the microstructure of fatigue crack growth. The presence of a ductile β phase bordering the α_2 phase (as in the heat treatment A condition) appears to be a critical requirement for improved resistance to fatigue crack growth. Davidson *et al.* [19] in a study of Ti–24 Al–11Nb (at %) showed that microcracks formed at the α_2/β interface and along slip lines. These microcracks form ahead of the crack tip and hence do not play a role in toughening; on the contrary, their existence is detrimental to the crack growth process. In their study of *in-situ* crack growth mechanisms they showed that the β phase was responsible for crack bridging, crack deflection and crack blunting.

4.2. Elevated temperature fatigue crack growth

Kerans [5] in a study of the cyclic fatigue of binary Ti_3Al without any Nb has indicated that there is a pronounced decrease in fatigue life above 700 °C. This result was attributed to differences in compatibility stresses between grains that deform and those that do not. This difference arises due to the fact that grains that are properly oriented for slip based on the $\frac{a}{3}\langle 1120\rangle$ slip vector deform extensively while grains not properly oriented do not. Balsone *et al.* [20] in their study of fatigue behaviour at 650 °C and 750 °C showed that as the frequency of testing was decreased, the crack growth rate per cycle was increased. They postulated that at frequencies between 0.001 and 20 Hz the Ti–24Al–11Nb alloy exhibited a mixture of time-dependent and cycle dependent behaviour. However, at frequencies large than 20 Hz a purely cycle dependent behaviour was observed. In their study, tests conducted in air showed a much higher crack growth rate compared to tests in vacuum at 650 °C. Mall *et al.* [21], in fatigue tests involving the addition of hold times to a 0.1 Hz, $R = 0.3$ cycle, showed an increase in growth rate with an increase in hold time. They reported that the addition of 30 and 120 s hold times resulted in doubling the cyclic crack growth rate while hold times of 300 and 600 s tripled the growth rate. The presence of a time dependent fatigue behaviour is indicative of the influence of the environment and creep processes at elevated temperature.

Fatigue crack growth tests were conducted at 700 °C for heat treatments A and B at a frequency of 20 Hz and an R ratio of 0.1. Fig. 15 shows the da/dN versus ΔK plots. It is apparent that the microstructure does not play a significant role on fatigue crack growth rates at 700 °C, as reflected by the nearly identical crack growth rates in all regimes. Crack growth was observed to occur across both the α_2 and β phases with very little crack branching. The fracture surfaces indicated that the crack growth was transgranular. Fig. 16 (a, b) are scanning electron micrographs of fracture surface of specimens A and B1 tested at 700 °C. At this temperature both the α_2 and β phases are ductile and appear to deform in a similar fashion. A comparison of Fig. 12 and Fig. 15 indicates that the apparent ΔK_{th} increases from 6 MPa m$^{1/2}$ at room temperature to about 10 MPa m$^{1/2}$ at 700 °C for microstructure A. The origin of this increase of

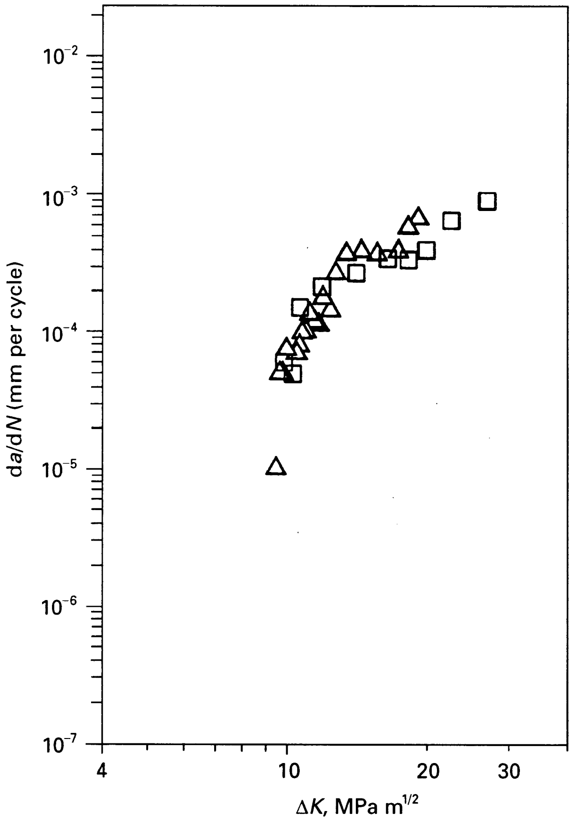

Figure 15 Fatigue crack growth rate da/dN as a function of stress intensity factor range ΔK at 700 °C for Ti–24Al–11Nb alloy subjected to prior exposure at 800 °C for 0 (□) (heat treatment A) and 100 h at 800 °C followed by an air cool ((△) heat treatment B). Both tested at a frequency of 20 Hz and $R = 0.1$.

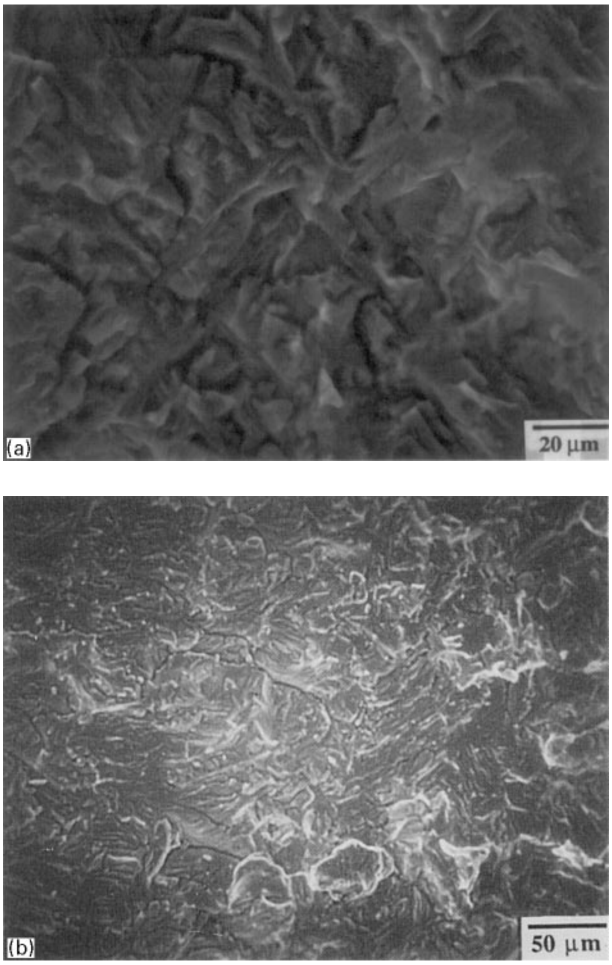

Figure 16 Scanning electron micrograph of the fracture of (a) Heat treatment A and (b) Heat treatment B tested in fatigue at 700 °C at a frequency of 20 Hz and $R = 0.1$.

resistance to crack growth in the near threshold region may arise from two sources. (i) The inherent resistance of the Ti–24Al–11Nb alloy to crack growth is increased due to the increased temperature. (ii) Enhanced amounts of oxide induced closure exists at 700 °C. Offsetting these beneficial aspects is the possibility of embrittlement by oxygen which stabilizes the α_2 phase.

One of the beneficial aspects of elevated temperature fatigue is the creation of oxide corrosion products on the newly created fracture surfaces in the wake of the crack tip. The factors for the formation of the oxide are the presence of a fresh fracture surface, elevated temperatures and the fretting action of the wake of the crack creating fresh regions for oxidation. The presence of this oxide product leads to premature closure or contact of the crack faces, leading to a much smaller ΔK_{eff}. This effect is predominant at low stress ratios and near the threshold for crack growth. It has been recently shown by Sobeyejo *et al.* [22] that oxide induced closure plays a significant role in elevated temperature crack growth behaviour in Ti–48 Al (wt%). They showed that at 700 °C at an R ratio of 0.1 little or no crack growth was observed at $\Delta K = 11$ MPa m$^{1/2}$ in Ti–48 Al. They showed that the fracture surface oxide layer thickness as measured by Auger electron spectroscopy was generally greater than the minimum crack opening displacement. It is generally accepted that Ti–24Al–11Nb is more susceptible to oxidation compared to Ti–48Al, hence it can be inferred that the presence of an oxide residue can provide larger values of K_{cl}, leading to apparent improvements of near threshold fatigue crack growth resistance.

5. Tensile and stress rupture failure

The stress rupture results for both 649 and 760 °C are plotted in Fig. 17. Summaries for these tests are provided in Tables II and III, including comments regarding prodominant failure modes and microstructural changes that were observed. Specific discussion regarding these results are detailed in subsequent sections. With regard to the tensile properties, two tests each were conducted in vacuum at both 649 and 760 °C. These results are tabulated in Table IV.

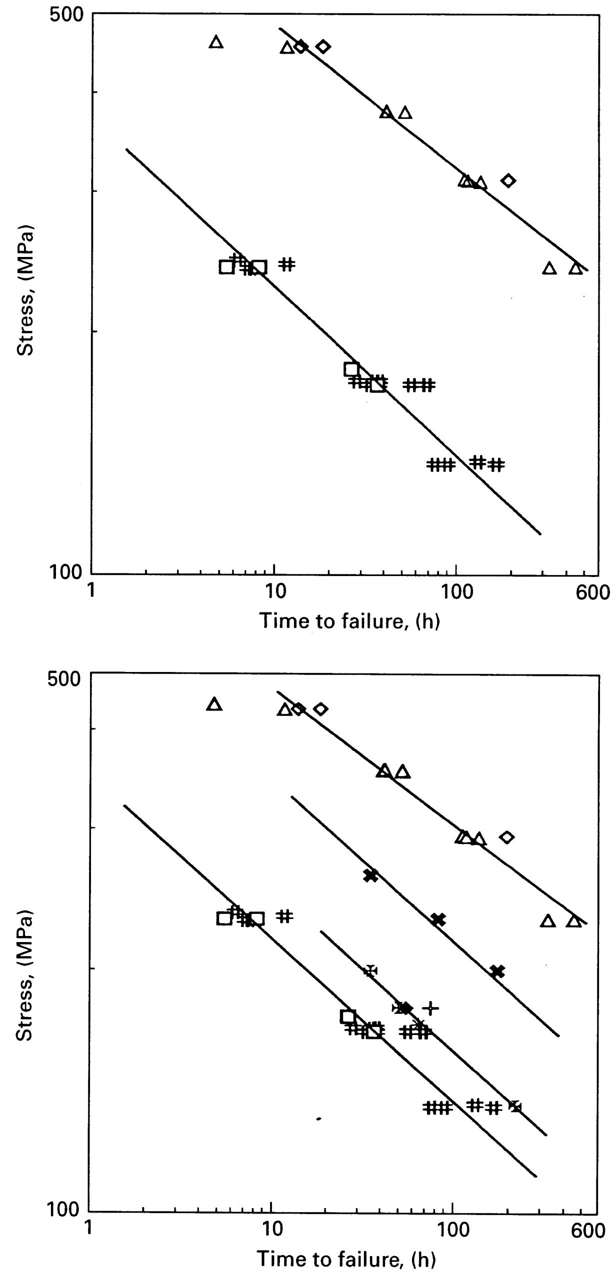

Figure 17 (a) Time to failure under stress rupture testing for Ti–24Al–11Nb at the environmental conditions; (#) 760 °C in air. (□) 760 °C vacuum, (△) 649 °C in air and (◇) 649 °C in vacuum. (b) As for (a) with the extra data of Balsone [24] included, the extra environmental conditions are; (X) 700 °C in air, (⊛) 750 °C in air (*) 750 ° C in (air-100/750), (+) 750 °C (air–500/750) and (◆) 750 °C in vacuum.

5.1. Stress rupture tests at 760 °C in air

All specimens subjected to stress rupture tests in air at 760 °C were heat treated to condition D (Table I) prior to testing. Even though the data in Fig. 17 indicates a large scatter band in the time to failure at each stress level, a logarithmic correlation exists between stress and time to failure. There is little difference in the time to failure between specimens tested in air and in vacuum. Based on these results it appears that oxidation and oxygen embrittlement do not play an important role in influencing stress rupture life at 760 °C.

The fracture surfaces of the samples exhibited three distinctive types of failure: (i) intergranular, (ii) transgranular, and (iii) final rupture. The intergranular and transgranular behaviour refer to prior β grains and correspond to time dependent stable crack growth. The final rupture was also transgranular but corresponded to final unstable crack growth. There appears to be a correlation between the time to failure and the mechanism of failure. Specimens that exhibited a transgranular mode of failure also had long lives while specimens that exhibited intergranular failure had short lives. Table V details the relationships between the types of failure and the stress rupture lifetimes of specific specimens tested in air at 760 °C. Fig. 18 depicts the fracture surface of a specimen tested in air at 760 °C at a stress level of 138 MPa, which had a lifetime of 132 h. The crack initiated transgranularly

TABLE II Summary of the 649 °C stress rupture test results

Nominal applied stress (MPa)	Test environment	Average time to failure (h)	Predominant failure mode	Microstructural change
455	Air	8.3	TG	Not Noticeable
455	Vacuum	16.3	IG	Not Noticeable
378	Air	45.1	TG	Some
310	Air	121.8	TG	Some
310	Vacuum	192.8	IG	Some
241	Air	386	TG	Some
Tensile	Vacuum	N/A	IG	Not Noticeable

IG intergranular failure.
TG transgranular failure.

TABLE III Summary of 760 °C stress rupture test results

Nominal applied stress (MPa)	Test environment	Average time to failure (h)	Predominant failure mode	Microstructural change
241	Air	8.2	IG	Substantial
241	Vacuum	6.9	IG	Substantial
172	Air	34.7	IG	Substantial
172	Air	64.6	TG	Substantial
172	Vacuum	31.7	IG	Substantial
137	Air	82.9	IG	Substantial
137	Air	148.7	TG	Substantial
Tensile	Vacuum	N/A	IG	Substantial

IG intergranular failure.
TG transgranular failure.

TABLE IV Tensile strength of Ti–24Al–11Nb

Test temperature (°C)	Ultimate tensile strength (MPa)
649	662
760	483

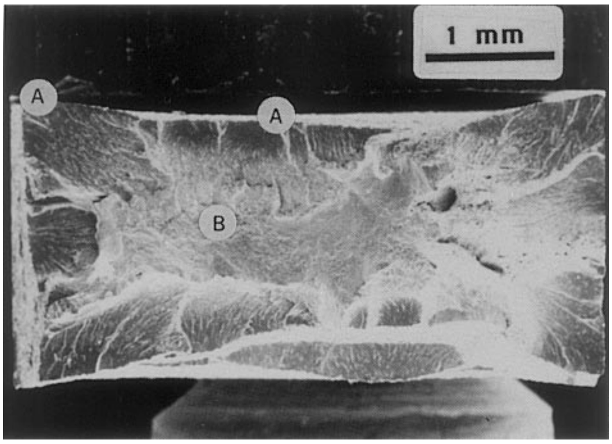

Figure 18 Fracture surface of a stress rupture specimen tested in air at 760 °C at a stress level of 138 MPa, which had a lifetime of 132 h. A-transgranular initiation site, B-final rupture area.

at the point marked A and the predominant mode of failure was by transgranular crack growth. Fig. 19 shows the fracture surface of a specimen tested in air at 760 °C at a stress of 137 MPa, which had a lifetime of 90 h. Three characteristic regions are visible. Regions marked A had a golden yellow appearance which corresponded to extensive oxidation and appeared to be crack initiation sites. Regions marked B were regions of transgranular crack growth and had a purple colour. This purple colour indicated that oxidation had just begun and hence this region corresponds to the final rupture failure. Regions marked C were blue in colour and corresponded to stable crack growth and appeared to be largely intergranular in nature. In the intergranular region, the direction of crack growth was hard to characterize, as the surface had extensive tearing and microvoid coalescence with no unique orientation. Specimens tested at the intermediate stress of 172–174 MPa also exhibited a correlation between failure mode and stress rupture life similar to specimens tested at the lower stress of 138 MPa. As indicated in Table III, at high stress levels of 241 MPa the time to failure was typically very short and cracks propagated entirely in an intergranular fashion, except for the final rupture area which was transgranular. Fig. 20 shows a 240 MPa stress rupture specimen tested at 760 °C in air with a 7.2 h lifetime. Based on the above results it can be inferred that the transgranular crack mode is oxidation initiated and intergranular crack growth is primarily caused by a creep mechanism. This is evident by noting that at (i) short lifetime, highly stressed specimens have a total intergranular fracture surface and (ii) the area of transgranular stable crack growth increases with increasing time at temperature.

In conventional α/β titanium alloys it has been shown that prior β boundaries are heterogeneous nucleation sites for α plates resulting in grain boundary α [23]. In $\alpha_2 + \beta$ intermetallics a similar behaviour is exhibited as shown in Fig. 10. At the grain boundary region there appears to be a large number of oriented

TABLE V Relationship between failure mode and stress rupture lifetimes for selected specimens tested at 760 °C in air

Applied stress (MPa)	Intergranular failure area (%)	Transgranular failure area (%)	Final rupture area (%)	Stress rupture life (h)
137	53	7	40	76.3
137	33	16	51	89.5
138	0	38	62	131.5
137	0	63	37	165.8
172	4	30	66	68.3
174	71	13	16	28.3
172	4	33	63	68.8

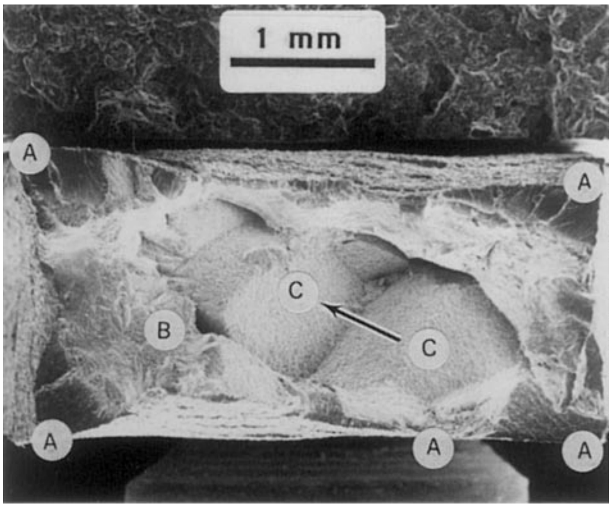

Figure 19 Fracture surface of a stress rupture specimen tested in air at 760 °C at a stress level of 137 MPa, which had a lifetime of 90 h. A-initiation site, B-final rupture area, C-stable crack growth areas.

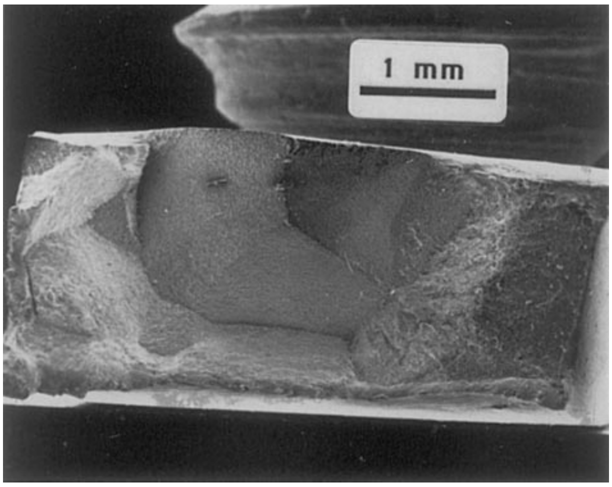

Figure 20 Fracture surface of a stress rupture specimen tested in air at 760 °C at a stress level of 240 MPa, which had a lifetime of 7.2 h.

α_2 platelets. In regions away from the grain boundary the α_2 and β phases exhibit an orientation relationship of the kind, $(0001)_{\alpha_2} \parallel (110)_\beta$, $\langle 1120\rangle_{\alpha_2} \parallel \langle 111\rangle_\beta$ and $(1010)_{\alpha_2} \parallel (112)_\beta$, $\langle 1120\rangle_{\alpha_2} \parallel \langle 111\rangle_\beta$. These provide for continuity of slip and inhibit void formation. At the grain boundaries the neighbouring laths of α_2 phase do not exhibit an orientation relationship with each other. This leads to slip incompatibility and void nucleation and growth preferentially at the grain boundary.

The prior β grain size is of the order of 1–2 mm which is about half the size scale of the thickness of the specimen. Hence the orientation of the grains with respect to the loading axis plays an important role in determining rupture life. For specimens where a critical shear stress is not achieved at the grain boundary, transgranular crack growth is initiated which progresses in a stable manner until a grain that is oriented for grain boundary sliding is reached. Then subsequent crack growth is intergranular in nature.

The surfaces of the specimens tested in air at 760 °C were also examined away from the fracture region to examine the crack initiation mechanism. Fig. 21a shows the surface of a 172 MPa specimen tested in air at 760 °C which failed by a combination of grain boundary sliding and transgranular cracking. Extensive transgranular cracks oriented perpendicular to the loading direction are seen in grain B. Regions C and D are shown in better detail in Fig. 21(b, c). Region C clearly shows grain boundary sliding type of crack initiation. In region D a sequence of cracks appear at the prior β grain boundary. This indicates that both intergranular and transgranular cracking may be aided by surface oxidation.

When tested air at 760 °C extensive microstructural changes were observed. Fig. 22(a) is a post test microstructure of a specimen tested in air at 760 °C at a stress of 137 MPa, which had a failure time of 90 h. Fig. 22b is a sample placed in air at 760 °C with no stress for 90 h. Fig. 22a clearly shows spherodization of the β phase near the fracture surface whereas Fig. 22b just shows a little coarsening of the microstructure. It is clear that the application of stress accelerated the breakup of the β phase and aids in its spherodization.

5.2. Stress rupture tests at 760 °C in vacuum

As noted in the previous section, all stress rupture tests conducted a 760 °C were performed on specimens which had been heat treated to condition D (Table I). The test data plotted in Fig. 17 showed that the test environment (air vs. vacuum) made little difference in the time to failure. With regard to failure modes, the fracture surfaces of all the vacuum tested samples were intergranular except for the final rupture area which was transgranular. Fig. 23a is a micrograph of the fracture surface of a specimen tested in a vacuum at 760 °C with a stress of 241 MPa, which had a lifetime of 8 h. All the creep crack growth was intergranular

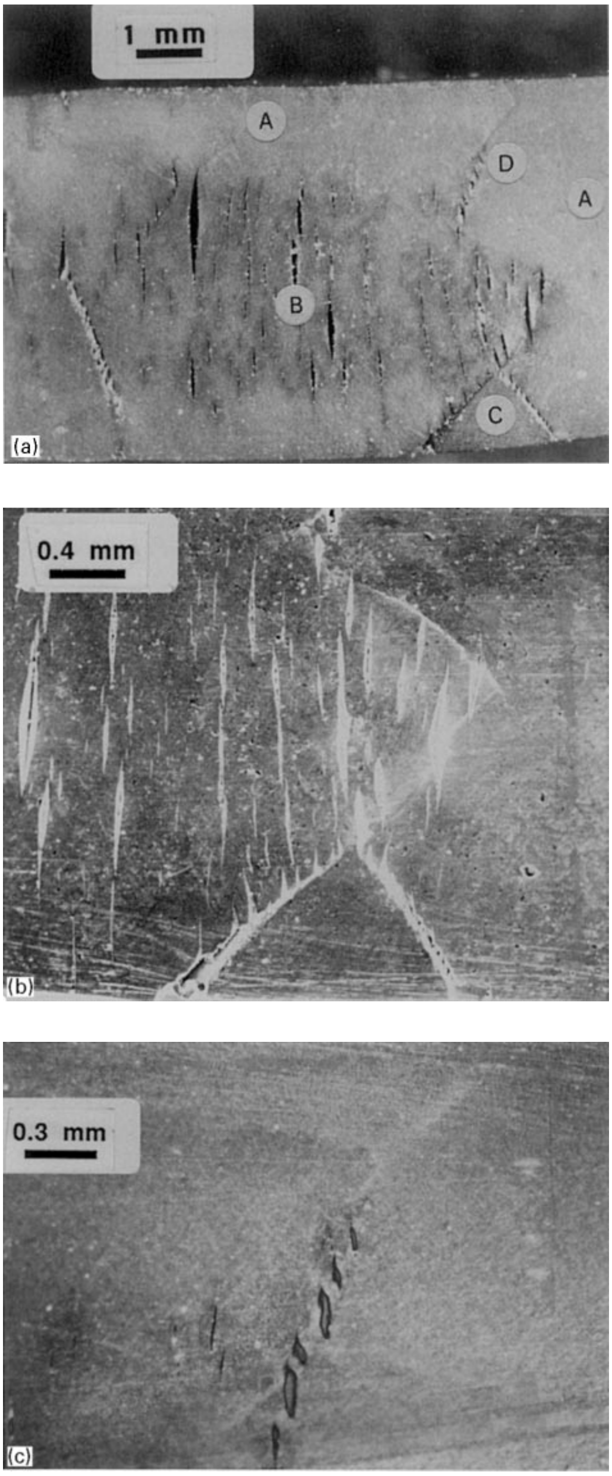

Figure 21 Stress rupture specimen tested in air at 760 °C at a stress level of 172 MPa and a lifetime of 68 h. (a) Optical micrograph near the fracture surface. (b, c) Higher magnification micrographs of regions marked C and D.

with the final rupture being transgranular. Unlike the air tested specimens, the primary surface characteristic of the vacuum tested specimens is the sliding of the prior β grains. A typical example is shown in Fig. 23b which is the same sample shown in Fig. 23a. In addition to grain boundary cracks slip traces parallel to the loading direction can be seen near the fracture region. These traces do not appear to be due to oxidation, as no surface discolouration was seen.

Other creep tests performed by Balsone [24] also indicated a transgranular cracking when tested in air.

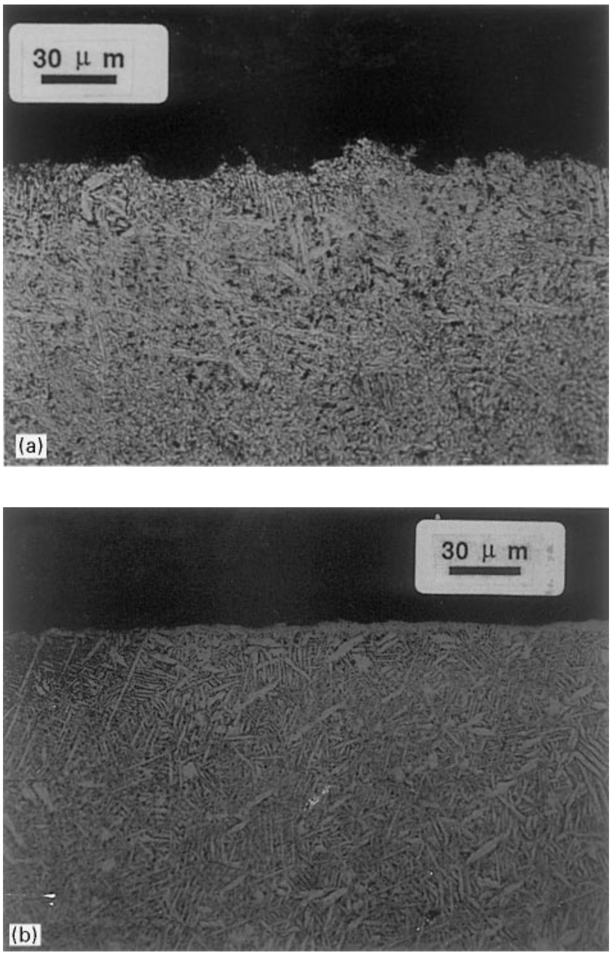

Figure 22 (a) Post test microstructure of a stress rupture specimen tested in air at 760 °C at a stress level of 137 MPa and a failure time of 90 h. (b) Another specimen placed in air at 760 °C for 90 h without any stress.

Balsone [24] attributed the transgranular cracking in creep specimens in air to oxygen embrittlement. Results obtained by Balsone [24] are plotted together with our results in Fig. 17. It is clear that there is a good match between Balsone's data and ours. When tested in vacuum of 1×10^{-5} Torr, results by Balsone [24] indicated no transgranular slip or cracking but only grain boundary relief. Current results at a vacuum of 1×10^{-6} Torr indicate the formation of transgranular slip traces on the surface in a direction normal to the loading axis. Extensive changes in the microstructure are seen due to the creep testing at 760 °C. Fig. 23c is the optical micrograph of the same specimen near the fracture region clearly showing extensive breakup of the continuous β phase even after only 8 h at temperature. It is clear that the presence of a tensile stress coupled with elevated temperature accelerates the breakup and spherodization of the β phase.

5.3. Stress rupture tests at 649 °C in air and in vacuum

At the lower test temperature of 649 °C, four different stress levels of 455, 379, 310 and 241 MPa were employed in stress rupture testing. Fig. 17 indicates that stress rupture tests in vacuum at 649 °C consistently

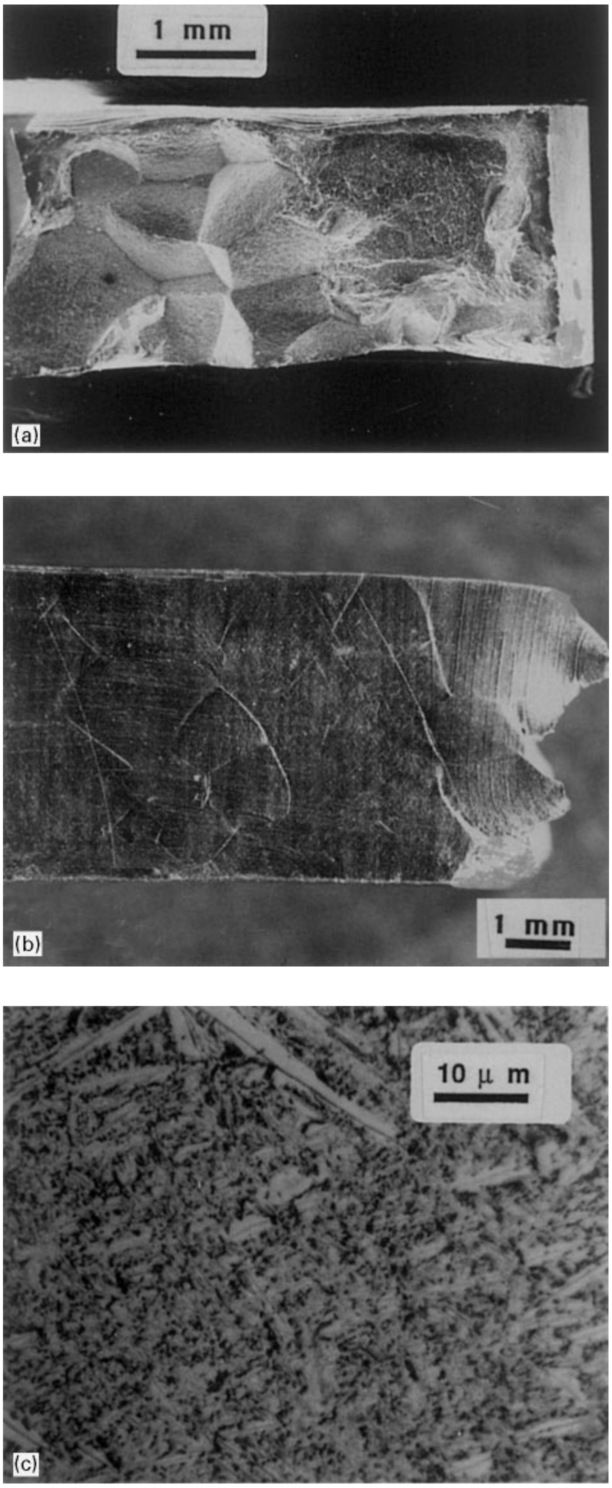

Figure 23 (a) Fracture surface of a stress rupture specimen tested in vacuum at 760 °C at a stress of 241 MPa, which had a failure time of 8 h (b) Low magnification optical micrograph of the surface of the specimen. (c) High magnification optical micrograph of the microstructure near the fracture region.

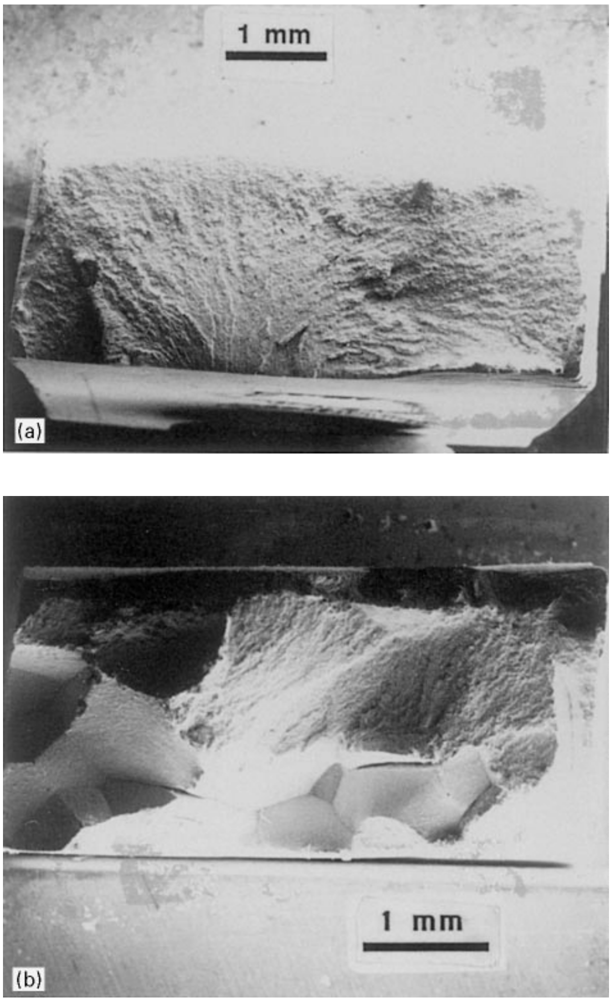

Figure 24 (a) Fractograph of a stress rupture specimen tested in air at 649 °C at a stress of 379 MPa, which has a failure lifetime of 41 h. (b) Fractograph of a stress rupture specimen tested in air at 649 °C at a stress of 455 MPa, which had a failure time of 14 h.

yielded longer lives than specimens tested in air. All specimens tested in air at 649 °C consistently failed in a brittle transgranular fashion with the crack typically initiated on the surface. Fig. 24(a) is a fractograph of a specimen tested in air at 649 °C at a stress of 379 MPa, which had a failure time of 41 h. The fracture mechanism in the steady state crack growth region was typically by quasi-cleavage with little evidence of ductility. The final rupture was caused by a combination of ductile tearing and quasi-cleavage. The complete absence of any intergranular fracture indicates that this temperature is below the equicohesive temperature where the grain boundaries are stronger than the matrix within the grains. Hall [25] presented data showing a ductile–brittle transition occurring in this alloy at approximately 370 °C, with the ductility becoming relatively constant in the temperature range of 535–649 °C (the upper range of this data).

When tested in vacuum the failure mechanism was always intergranular in the stable creep crack growth regime and transgranular crack growth in the final rupture. Fig. 24b is a fractograph of a specimen tested in air at 649 °C at a stress of 455 MPa, which had a failure time of 14 h. It appears that oxygen embrittles the matrix and raises the equicohesive temperature when tested in air. However in vacuum the grain boundaries are still weaker than the matrix at 649 °C and the equicohesive temperature is below 649 °C when tested in the absence of air. Some of the detrimental effects of testing in air become apparent when the surfaces of the air and vacuum tested samples are examined. Fig. 25a is the surface of a specimen tested in air at 649 °C at a stress of 241 MPa, which had

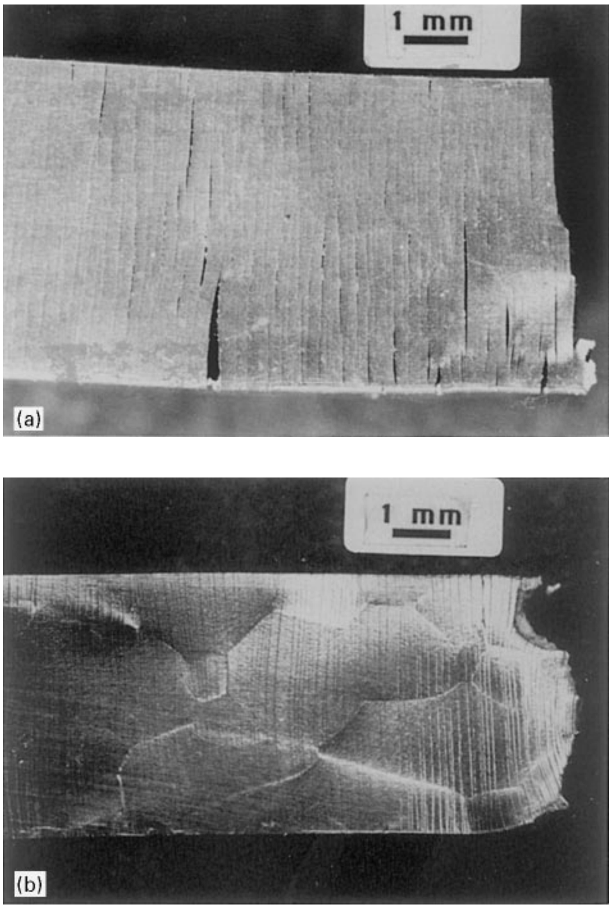

Figure 25 (a) The surface of a stress rupture specimen tested in air at 649 °C at a stress of 241 MPa, which has a failure lifetime of 449 h. (b) The surface of a stress rupture specimen tested in vacuum at 649 °C at a stress of 310 MPa, which had a failure time of 193 h.

a lifetime of 449 h and Fig. 25b is the surface of a specimen tested in vacuum at 649 °C at a stress of 310 MPa, which had a lifetime of 193 h. Extensive transgranular cracks perpendicular to the loading axis were observed that sometimes ran completely across the surface in specimens tested in air. This behaviour is not unlike specimens tested in air at 760 °C in air. The vacuum tested specimens also behaved in a fashion very similar to the vacuum tested specimens at 760 °C, exhibiting grain boundary surface relief and slip traces near the fracture surface. The extent of microstructural changes at 649 °C was significantly lower than at 760 °C, and these changes appear to be driven by the time at temperature rather than the stress applied.

6. Conclusions

The following general conclusions can be drawn from this work regarding the fatigue crack growth and stress rupture behaviour of Ti–24Al–11Nb.

(i) Prolonged exposure at 800 °C, leads to the break up of the continuous β phase. The coarse Widmanstätten microstructure changes to a microstructure of primarily α_2 phase with particles of the β phase scattered in it.

(ii) Prolonged heat treatment at 800 °C reduces the resistance to fatigue crack growth at room temperature. This was attributed to dissolution of the β phase surrounding the α_2 laths boundaries. The best fatigue resistance was associated with the microstructure that had not been subjected to 800 °C exposure and had a continuous layer of ductile β phase around the brittle α_2 phase.

(iii) Long term exposure at 800 °C does not play much of a role in determining fatigue crack growth behaviour at 700 °C. Crack growth occurs through both the α_2 and β phases with a straight crack path.

(iv) With stress rupture tests at 760 °C in air, the failure was a mixture of transgranular and intergranular crack growth. Transgranular failure promoted longer lives compared to intergranular failure. When tested in vacuum the primary mode of failure was intergranular in nature. There was little difference in the time to failure between specimens tested in air and vacuum.

(v) At 649 °C the time to failure in vacuum was always longer compared to tests in air. When tested in air at 649 °C the primary model of creep crack growth was a brittle transgranular mode while the vacuum tested specimens always exhibited intergranular failure.

Acknowledgements

Support provided by Lockheed Fort Worth Division, the Mechanical Engineering Department and Materials Science and Engineering Program at University of Texas at Arlington is appreciated.

References

1. S. M. L. SASTRY and H. A. LIPSITT, *Metall. Trans. A* **8** (1977) 299.
2. *Idem., ibid.* **8** (1977) 1543.
3. *Idem., Acta Metall.* **25** (1977) 1279.
4. H. A. LIPSITT, D. SHECHTMAN, and R. E. SCHAFRIK, *Metall. Trans. A* **11** (1980) 1369.
5. R. J. KERANS, *Idem.* **15** (1984) 1721.
6. R. G. ROWE, *High Temperature Aluminides and Intermetallics.*, Sym. Proc., October 1–5, 1989, Indianapolis edited, S. H. Whang, C. T. Liu and D. P. Pope and J. O. Stiegler, TMS-AIME, (Pittsburg, PA, 1990) p. 460.
7. Y.-W. KIM and F. H. FROES, *Ibid*, p. 485.
8. P. B. ASWATH and S. SURESH, *Materials Science and Engg.* **A114** (1989) L5-L10.
9. P. B. ASWATH, W. O. SOBOYEJO and S. SURESH, *Fatigue* '90 edited H. Kitagawa and T. Tanaka, eds., (Materials and Components Engineering Publications, Ltd., Warley, U.K., Vol. III, (Honolulu, Hawaii, July 15–20, 1990)) pp. 1941–1946.
10. P. B. ASWATH and S. SURESH, *Elevated Temperature Crack Growth*, edited by S. Mall and T. Nicholas., ASME Winter Annual Meeting, Dallas, Nov. 25–30, (ASME, New York, 1990), pp. 69–77.
11. P. B. ASWATH, "Micromechanics of Quasi-Static and Fatigue Crack Growth in Titanium Aluminides", Ph.D. Thesis, Brown University, (1990).
12. P. B. ASWATH and S. SURESH, *Metall. Trans. A.* **22** (1991), 817.
13. D. BANERJEE, A. K. GOGIA, T. K. NANDI and V. A. JOSHI, *Acta Metall.* **36** (1988) 36.
14. S. SURESH, *Engg. Fracture. Mechanics.* **21** (1985) 453.
15. R. STRYCHOR, J. C. WILLIAMS and W. A. SOFFA, *Metall. Trans. A* **19** (1988) 225.
16. D. BANERJEE, A. K. GORGIA and T. K. NANDY, *Ibid.* **21** (1990) 627.
17. S. SURESH, *Ibid.* **14** (1983) 2375.

18. *Idem. ibid.* **16** (1985) 249.
19. D. L. DAVIDSON, K. S. CHAN and J. LANKFORD, "Crack Growth Processes at Elevated Temperatures in Advanced Materials", AFOSR Annual Report for 1989, under contract F49620-89-C-0032, January, 1990.
20. S. J. BALSONE, T. NICHOLAS, D. C. MAXWELL and M. KHOBAIB, *Elevated Temperature Crack Growth.* edited by T. Nicholas and S. Mall (ASME., New York, NY, (1990)) pp. 87–91.
21. S. MALL, T. NICHOLAS, D. G. BURGESS, and J. J. PERNOT, *Engg. Fract. Mech.* (submitted).
22. W. O. SOBEYEJO, J. E. DEFFEYES and P. B. ASWATH, *Mat. Sci. and Engg. A***138** (1991) 95.
23. H. MARGOLIN, *Met. Trans. A* **13** (1982) 2191.
24. S. J. BALSONE, *Oxidation of High Temperature Intermetallics*, edited by J. Doychak and T. Grobstein, (TMS-AIME (1988)) pp. 219–234.
25. J. HALL, *Ibid.* pp. 235–240.

Received 28 March 1995
and accepted 20 November 1995